

Geophysical Research Letters

RESEARCH LETTER

10.1029/2021GL093659

Key Points:

- Anisotropy markedly affects wormholing dynamics, medium permeability evolution, and the optimum injection rate
- Anisotropy controls wormhole competition and their characteristic separation distance, wormhole shapes and tendency to develop side-branches
- Similarities and differences to viscous fingering and other unstable growth processes are analyzed

Supporting Information:

Supporting Information may be found in the online version of this article.

Correspondence to:

P. Szymczak and R. Roded,
piotr.szymczak@fuw.edu.pl;
roi.roded@mail.huji.ac.il




Citation:

Roded, R., Szymczak, P., & Holtzman, R. (2021). Wormholing in anisotropic media: Pore-scale effect on large-scale patterns. *Geophysical Research Letters*, 48, e2021GL093659. <https://doi.org/10.1029/2021GL093659>

Received 8 APR 2021

Accepted 14 MAY 2021

Wormholing in Anisotropic Media: Pore-Scale Effect on Large-Scale Patterns

R. Roded¹ , P. Szymczak² , and R. Holtzman³ 

¹Hydrology and Water Resources, The Hebrew University, Jerusalem, Israel, ²Institute of Theoretical Physics, Faculty of Physics, University of Warsaw, Warsaw, Poland, ³Fluid and Complex Systems Research Centre, Coventry University, Coventry, UK

Abstract The formation of dissolution conduits by focused reactive flow (i.e., wormholing) in anisotropic media is studied using a pore network model. Simulations reveal a significant effect of anisotropy on wormholing dynamics and medium permeability evolution. Particularly, anisotropy controls wormhole competition and their characteristic spacing. It also affects the flow through the individual wormholes and their shapes, and consequently, shifts the optimum injection rate at which breakthrough is achieved at a minimal expense of reactant. For anisotropic media with low transverse pore conductivities, wormhole distribution ceases to be scale-invariant and pronounced side-branches develop. Wormholing is further compared to viscous fingering in an anisotropic network, and other unstable growth processes of similar underlying dynamics. Despite several similarities, few important differences are identified. Our findings contribute to the understanding of wormholing in geological media and demonstrate how pore-scale features can fundamentally affect the emergence of large-scale morphologies.

Plain Language Summary The flow of corrosive fluids in an aquifer (e.g., acidic water in limestone) can become focused in conductive pathways leading to the formation of pronounced dissolution conduits—wormholes. Wormholes can form across a large range of scales, from microns to the extended systems of karst conduits. Wormholing patterns evolve by competitive dynamics: Longer wormholes drain more flow and hence grow faster, increasing their conductivity, in turn focusing even more flow. In the meantime, shorter wormholes become devoid of reactant and stop growing. This results in a hierarchical distribution of wormhole lengths, with many small and only a few long ones. Here, using a numerical model, we study wormholing in anisotropic media characterized by different permeabilities along different directions—a common feature of geological media. We find that anisotropy markedly affects wormhole dynamics and the evolution of overall medium permeability. Particularly, anisotropy affects wormhole competition and thus their number, shapes, and branching. Wormholing is further compared to other pattern-forming processes in nature, and similarities and differences are analyzed. These findings contribute to the understanding of wormholing, with implications to subsurface flow-related processes such as karst and contaminant migration. The results demonstrate how micro-scale features control the large-scale morphology.

1. Introduction

Focused reactive flow and dissolution in fractured or porous media leads to the emergence of highly conductive dissolution conduits, so-called “wormholes” (Daccord et al., 1993; Hoefner & Fogler, 1988). Dissolution conduits are prevalent in subsurface karst, and can form extended speleological systems (Dreybrodt et al., 2005; Palmer, 1991). Wormholes are also important in several other applications, including CO₂ geo-sequestration (Deng et al., 2016), risk assessment of groundwater contamination (Fryar & Schwartz, 1998) or stimulation of petroleum reservoirs (Panga et al., 2005).

The underlying mechanism involves positive feedback between reaction and transport—the pathways that focus the reactive flow dissolve preferentially, increasing their conductivity, and in turn focusing more flow. Concurrently, shorter wormholes are progressively drained and screened off by the longer wormholes, and ultimately cease to grow, resulting eventually in the appearance of hierarchical, scale-invariant distribution of wormhole lengths (Szymczak & Ladd, 2006). Similar competitive dynamics and emergence of

hierarchical structures are observed in various other unstable growth processes in nature, with examples ranging from viscous fingering (Roy et al., 1999) to crack propagation in brittle solids (Huang et al., 1997) and side-branches growth in crystallization (Couder et al., 1990).

The importance of wormholing and its intriguing physics motivated intensive research, in particular on the emergence of reactive-infiltration instabilities (Aharonov et al., 1995; Chadam et al., 1986), wormhole formation and competitive dynamics (Budek & Szymczak, 2012; Szymczak & Ladd, 2006), and the effects of medium heterogeneity (Hanna & Rajaram, 1998; Upadhyay et al., 2015). However, the effect of pore-scale anisotropy on the dissolution patterns has received only minor attention (e.g., Lai et al., 2016; Schwalbert et al., 2017), despite its prevalence in rocks (Clavaud et al., 2008, and references therein), often induced by in-situ differential stress (Bruno, 1994; Kang et al., 2019). Additionally, anisotropic void-space is characteristic of fractured media at scales ranging from a single fracture to the field-scale (Bonnet et al., 2001; Sahimi, 2011), and often is very pronounced (Barton, 2006). Furthermore, previous studies of similar unstable growth processes have shown that anisotropy can have a substantial effect on the dynamics and pattern formation (Ben-Jacob et al., 1985; Budek et al., 2015; Couder et al., 1990).

In this study, we investigate the effects of pore-scale anisotropy on wormholing dynamics and permeability evolution using a pore network model. We find that anisotropy strongly affects wormhole competition, their characteristic spacing, and shapes. Additionally, we highlight similarities and differences with viscous fingering in an anisotropic network of channels (Budek et al., 2015). The findings emphasize how pore-scale phenomena and microscopic characteristics of the medium can govern the formation of large-scale morphologies.

2. The Pore Network Model

To gain fundamental understanding of the effect of on wormholing, we use a 2-D numerical pore network model (PNM). PNMs are frequently used to represent dissolution in porous (e.g., Algive et al., 2010; Hoefner & Fogler, 1988; Nogues et al., 2013; Raouf et al., 2012) and fractured media (e.g., Dreybrodt et al., 2005; Perne et al., 2014). Despite their simplicity, PNMs capture the major characteristics of wormholing observed experimentally, including their structure and advancement rate, permeability evolution and the non-monotonic relationship between injection rate and fluid volume required for breakthrough (e.g., Budek & Szymczak, 2012; Fredd & Fogler, 1998; Wang et al., 2016).

In our model, the pore space is represented as connected cylindrical channels (of initially heterogeneous sizes) that are broadened by the dissolution (following e.g., Budek & Szymczak, 2012; Fredd & Fogler, 1998; Hoefner & Fogler, 1988; Wang et al., 2016). The nodes of the network (“pore junctions”) are assumed to be volumeless such that all the reaction takes place in the channels (“pores”) only (Figure S1 in the Supporting Information (SI)). This representation also resembles the 2-D network of conduits formed at the intersection of bedding plane with a subvertical fracture network, where karst systems evolution initiates (often called “inception horizon”; Dreybrodt, 1988; Filipponi et al., 2009; Frumkin et al., 2017).

The conservation equations for the fluid and solute are written for individual pores and nodes. These systems of equations provide the fluid fluxes, solute concentrations and mass of solid dissolved. Solute transport in the pores is assumed here to be dominated by advection in the axial direction (flow direction), whereas axial diffusion is neglected. This restricts the analysis to conditions where the pore-scale Péclet number, $Pe = \bar{v}l/D$, is sufficiently large, $Pe \gg 1$, common in natural processes and engineering applications (Ford & Williams, 2013; Niemi et al., 2017). Here l is the pore length, \bar{v} is the average fluid velocity and D is the diffusion coefficient. At pore surfaces, first-order dissolution reaction is considered. Such assumption is often applied to describe dissolution of limestone by acidic solutions (at pH ~ 3 or lower; Peng et al., 2015) and under natural conditions (karst, with pH ~ 6 ; Dreybrodt et al., 2005; Palmer, 1991), or of halite (Alkattan et al., 1997) and gypsum (Colombani, 2008) by water.

The separation of time-scales between fluid flow, solute transport, and dissolution allows us to use the quasi-static approach, treating the flow and concentration fields as stationary at each timestep. Then, following the dissolution in each timestep the geometrical properties are updated (see e.g., Bekri et al., 1995; Detwiler

& Rajaram, 2007; Lichtner, 1991). Below, the PNM and main equations are succinctly described; for detailed description see S1 in the SI and previous works (Budek & Szymczak, 2012; Roded et al., 2020).

2.1. Fluid Flow

For an incompressible fluid, steady-state fluid mass conservation at each node i yields

$$\sum_j q_{ij} = 0, \quad (1)$$

where q_{ij} is the volumetric flow rate through pore ij ($q_{ij} > 0$ indicates flow from node i to j), and the summation is over all neighboring nodes j . These flow rates are calculated using the Hagen-Poiseuille equation

$$q_{ij} = \frac{\pi r_{ij}^4}{8\mu l} \Delta p_{ij}, \quad (2)$$

where r_{ij} is the channel radius, μ is the fluid viscosity and $\Delta p_{ij} = p_i - p_j$ is the pressure drop between nodes, which are a distance l apart (l is constant throughout the network). The system of linear equations 1 and 2 is solved for the pressures at the nodes.

2.2. Reactive Transport and Dissolution

Dissolution is modeled assuming: (a) First-order reaction kinetics, (b) solute transport controlled by advection in the axial direction, and (c) by diffusion in the radial direction (from the bulk fluid to the mineral surface). With these assumptions, a 1-D solute conservation equation in each pore can be written in terms of the flow-weighted average concentration, c ,

$$q \frac{dc}{d\xi} = -2\pi r \lambda_{\text{eff}} c, \quad (3)$$

where ξ is the axial coordinate, and λ_{eff} is the effective reaction rate coefficient [L/T]. Using the known concentration of the pore inlet $c_{\text{in}} = c(\xi = 0)$, Equation 3 can be solved for the concentration profile along the pore

$$c(\xi) = c_{\text{in}} e^{-\frac{2\pi r \lambda_{\text{eff}} \xi}{q}}. \quad (4)$$

Substituting $\xi = l$ for the pore outlet, we note that the exponential decay of the concentration within the pore is controlled by

$$f(r, q) = \frac{s \lambda_{\text{eff}}}{q}, \quad (5)$$

where $s = 2\pi r l$ is the pore surface area. The effective reaction rate coefficient, $\lambda_{\text{eff}} = \lambda / (1 + g(r))$, incorporates the effect of transport on reaction, where λ is the surface reaction rate coefficient and the slowdown function $g(r)$ accounts for the extent by which dissolution rate within a single pore is hindered by the transport,

$$g(r) = \frac{\lambda 2r}{DSh}. \quad (6)$$

Here Sh is the Sherwood number, approximated by a constant value of $Sh = 4$ (Budek & Szymczak, 2012). The concentration at the nodes is then calculated using Equation 4 for each pore outlet, assuming complete mixing (Kang et al., 2019; Varloteaux et al., 2013). As noted previously (Kang et al., 2015), the assumption of complete mixing in junctions may affect reactant dispersion, which, in turn, can influence the dissolution patterns. A detailed investigation of this effect is beyond the scope of the present paper and is deferred for future research.

Conservation of solid mass together with the assumption that the pores are broadening uniformly along their length, provides the following expression for the change in radius during a timestep $\Delta \hat{t}$

$$\Delta r = \frac{r_0 \Delta \hat{t}}{(c_0/c_{\text{in}})} \frac{(1 - e^{-f})}{(1 + g)f}, \quad (7)$$

where c_0 is the concentration at the system's inlet, r_0 is the initial average radius, and \hat{t} is the dimensionless time

$$\hat{t} = \frac{\lambda t \gamma}{r_0}. \quad (8)$$

Here $\gamma = c_0/c_{\text{sol}}\theta$ is the acid capacity number, defined as the ratio between the number of molecules in a unit volume of mineral to the number of molecules of reactant in a unit volume of the incoming fluid, with θ accounting for the reaction stoichiometry. To account for a finite amount of soluble solid, once locally solid is fully dissolved between adjacent pores, these pores are merged (see Roded et al., 2018).

2.3. Dimensionless Groups

The dissolution rate of the pores is a function of f and g , with dependence on time arising through the radius, r , and flow rate, q . To characterize transport and reaction conditions, we use initial averaged values of f and g functions for the longitudinal pores, aligned in the main flow direction, x . This leads to the following definition of the dimensionless Damköhler number:

$$Da = \frac{s_0 \lambda}{\bar{q}(1 + G)}, \quad (9)$$

and the dimensionless transport parameter

$$G = \frac{\lambda 2r_0}{DSh}, \quad (10)$$

where s_0 and \bar{q} are the average surface area and inlet flow rate in longitudinal pores. Note that the Péclet number does not appear in these equations as diffusion effects in the axial direction are neglected ($Pe \gg 1$).

2.4. Simulation Setup

2.4.1. Initial and Boundary Conditions

We consider flow of fixed total volumetric rate, Q , and reactant concentration, c_0 , from the inlet to the outlet face. At the side walls, periodic boundary conditions for flow and transport are set. Concentration at the outlet nodes is calculated from solute mass conservation (Equation 4; free-flow boundary).

2.4.2. Network and Reactive Transport Conditions

We use a regular rectangular network and consider heterogeneity in pore volumes by drawing values from a lognormal distribution with relative standard deviation of 0.7, representative of the large characteristic variability in pore sizes of geological media (Sahimi, 2011). Anisotropy in the network is implemented by changing the average size of transverse pores, keeping the average size of the longitudinal pores constant in the different simulations. The anisotropy degree is defined as

$$S = \frac{a_y}{a_x}, \quad (11)$$

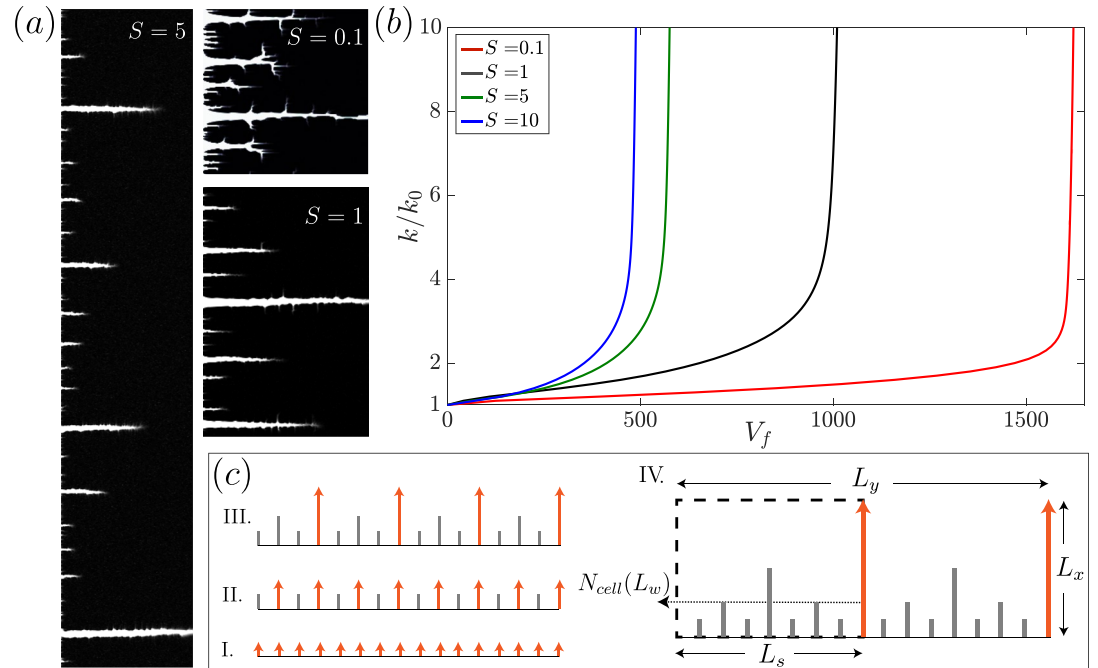


Figure 1. (a) Dissolution patterns in grayscale (white depicts fully dissolved areas) for different anisotropy degrees, S , and (b) the evolution of permeability k (normalized by its initial value, k_0) with injected fluid volume, V_f (scaled by the sample volume). (c) Schematics of the evolution of hierarchical growth pattern. Over time (advancing from I to IV), the number of active wormholes (orange) decreases, while the spacing between them increases. The dashed frame (IV) is the hierarchical cell, with an aspect ratio $\hat{L}_s = L_s/L_x$, and $N_{\text{cell}}(L_w)$ is the number of wormholes in the cell longer than L_w ; here $N_{\text{cell}}(L_w = 1/4L_x) = 4$. The patterns in (a) are shown for domains with $L_y/L_x > \hat{L}_s$.

where a is the average pore cross-sectional area, with subscript x and y denoting longitudinal and transverse pores. We use here S values of 0.1–10, to reflect the fact that anisotropy can be very pronounced (e.g., in the case of unidirectional tensile joints; Adler et al., 2013).

The network has 200 nodes in the x -direction, whereas the number of nodes in the orthogonal direction, y , depends on S . To allow uninhibited pattern formation, the computational domain must be sufficiently wide; this width, defined by the distance between the longest wormholes, depends on S , and thus we vary the aspect ratio when simulating different values of S (Section 3, Figure 1a).

In this study, we focus on the wormholing regime prevailing when the reaction rate is relatively fast, and thus consider values of $Da = 1$ and $G = 10$. To obtain statistically representative results for the heterogeneous media, results were averaged over 150 realizations.

3. Results and Discussion

The detailed microstructure of the porous medium can affect the manner in which reactive fluid is distributed within the void space and thus modify the dissolution patterns (Deng et al., 2018). Here, we show that anisotropy substantially changes the characteristic spacing between the wormholes (Figure 1a), and consequently the fluid volume required to attain a given permeability enhancement (Figure 1b). For narrow transverse pores (low S), the spacing between the wormholes is small and the reactant is spent on extending multiple wormholes. Conversely, for wide transverse pores (large S) dissolution is focused in a small number of competing wormholes, with more rapid permeability enhancement. Increasing S from 0.1 to 10, reduces by a factor of four the volume of reactive fluid, V_f , required to attain a 10-fold increase in permeability ($k/k_0 = 10$, where k_0 is the initial value), cf., Figure 1b.

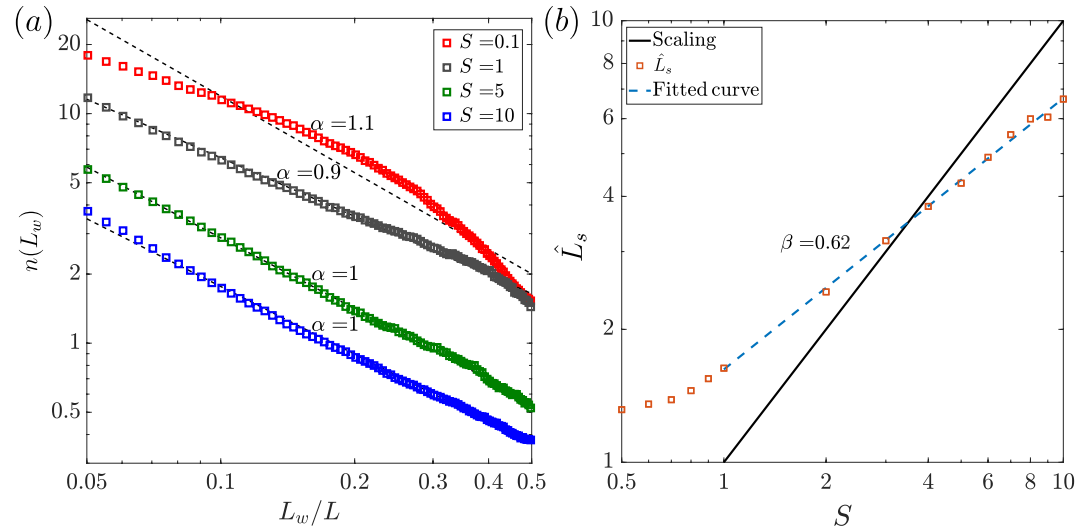


Figure 2. (a) The linear density of wormholes longer than L_w , $n(L_w)$. Wormhole distribution for anisotropy degree $S \gtrsim 1$, obeys a power-law with $\alpha \approx 1$ (Equation 12; fitted dashed black line). (b) Characteristic wormhole spacing, \hat{L}_s (orange squares), showing a fit to the power-law $\hat{L}_s \sim S^\beta$ with $\beta = 0.62$ (dashed blue line). The black line shows the dependence $\hat{L}_s \sim S$, which holds for Laplacian growth (e.g., viscous fingering). Wormholes shorter than $0.05L_x$ and longer than $0.5L_x$ were not taken into account in the distribution, the former because their length is influenced by the lattice discretization effects, and the latter because the selection process among the longest ones has not yet been concluded.

The underlying mechanism of wormhole growth involves competition between the wormholes for the available flow. Longer and more conductive wormholes progressively focus more flow at the expense of shorter ones. In return, an increased pressure ahead of the longer wormholes screens off the shorter ones, which ultimately cease to grow. This process perpetuates, leading to pattern coarsening: the separation between active (growing) wormholes increases while their number decreases (Figure 1c).

This competitive dynamics results in the appearance of hierarchical, scale-invariant distribution of wormhole lengths, obeying a power-law

$$n(L_w) \sim L_w^{-\alpha}, \quad (12)$$

where $n(L_w)$ is the linear wormhole density, $n(L_w) = N(L_w)/L_y$, with $N(L_w)$ being the total number of wormholes longer than L_w , normalized by injection face length, L_y , and $\alpha \approx 1$ (Szymczak & Ladd, 2006; Upadhyay et al., 2015). The exponent $\alpha \approx 1$ agrees with theoretical results on the scaling of dendrite growth driven by a Laplacian field (Krug et al., 1993). Here, we observe that while for $S > 1$ the length distribution indeed follows a power-law with $\alpha \approx 1$, for $S < 1$ the distribution ceases to be scale-free (Figure 2a). The different domain aspect ratios (Figure 1a) are chosen to be wider than the characteristic distance between the longest wormholes which has not yet screened each other, i.e., wide enough to accommodate at least one cell, which in turn depends on S (Figure 1c).

Interestingly, these findings are consistent with recent experimental results of viscous fingering of two immiscible fluids in an anisotropic network of microfluidic channels (Budek et al., 2015). The setup in Budek et al. (2015) can be described as a collection of zero-resistance dendrites (displacing fluid fingers of negligible viscosity) that interact through the Laplacian pressure field, with their growth proportional to the gradient ahead of their tips. An analogy between viscous fingering and wormholing can be made by replacing the continuous porosity field by a sharp transition: the wormholes approximated as fully dissolved and the matrix assumed completely undissolved. This analogy assumes that: (a) the pressure field in the undissolved rock satisfies the Laplace equation; (b) the hydraulic resistance of the wormholes is negligible in comparison to the matrix; and (c) wormhole growth speeds are proportional to the pressure gradient ahead of their tips (Cabeza et al., 2020).

The increase of the spacing between the wormholes and their lower density, $n(L_w)$, observed for wider and more conductive transverse pores ($S > 1$), is explained by enhanced interaction among the wormholes via the pressure field, increasing wormhole competition. However, when S is small, the interaction and selection are weaker, resulting in smaller separation distance and larger $n(L_w)$ (Figure 2a).

A longer wormhole of length L_w will screen neighboring shorter ones over a typical distance, L_s (Figure 1c). This distance can be obtained by dividing the width of the system, L_y , by the number of hierarchical cells in the system, ε ,

$$L_s = \frac{L_y}{\varepsilon}, \quad (13)$$

where ε is calculated using

$$\varepsilon = \frac{\bar{N}(L_w/L_x)}{N_{\text{cell}}(L_w/L_x)} \quad (14)$$

Here $\bar{N}(L_w/L_x)$ and $N_{\text{cell}}(L_w/L_x)$ are the number of wormholes that are longer than L_w at breakthrough, in the entire system and in the hierarchical cell, respectively. The latter is determined using Equation 12 as $N_{\text{cell}}(L_w/L_x) = (L_w/L_x)^{-1}$ (Figure 1c). Here, breakthrough is defined as the moment when the longest wormhole reaches the outlet. L_s can be scaled to provide the hierarchical cell aspect ratio, $\hat{L}_s = L_s/L_x$. Thus, the complete hierarchical distribution of the wormhole lengths can only be observed if the system is wide enough, $L_y/L_x \geq \hat{L}_s$.

In the case of viscous fingering on a rectangular network, both the numerical results and scaling analysis of the anisotropic Laplace equation suggest that the characteristic spacing scales linearly with S , $\hat{L}_s \sim S$, as long as $S \gtrsim 1$ (black line in Figure 2b; Budek et al., 2015). However, for wormholing, \hat{L}_s increases with S nonlinearly, obeying $\hat{L}_s \sim S^\beta$ with $\beta \approx 0.62$. This difference between the systems demonstrates that wormholing deviates from the simplified description of the model for dendrite growth in the Laplacian field and is a more intricate phenomenon. We attribute the power-law scaling to the effect of anisotropy on wormhole shape and their advancement velocity. The precise nature of this relationship remains the subject of future investigation. For $S < 1$, since the distribution is no longer hierarchical (see Figure 2a) the scaling relation is no longer valid.

By affecting wormhole spacing, the anisotropy also controls the flow rate drained through the individual wormholes, which in turn profoundly affects the wormhole shape (Fredd & Fogler, 1998; Golfier et al., 2002). To characterize the latter, we measure the wormhole aspect ratio, $A_{\text{wh}} = L_w/\rho$, defined as the ratio between wormhole length and its average width, ρ , calculated from the fully dissolved area (Figures 3a and 3b). We find that A_{wh} is inversely proportional to S . This can be rationalized by noting that as S decreases, the wormhole spacing and fluid velocity in individual wormholes decrease. This, in turn, leads to longer fluid residence times, substantial reactant concentration decay along the flow path (Figure 3b.1), and an enhanced role of the mass transfer to the wormhole walls (Steeffel & Lasaga, 1990; Szymczak & Ladd, 2009). As a result, the dissolution rate is largest near the inlet and decreases downstream, so that wormholes develop an elongated conical shape with relatively high A_{wh} (Figures 3a and 3b.1).

Conversely, for large S and fast flow, reactivity at the tip remains high and wormholes attain a more linear shape (so-called “dominant wormholes,” Fredd & Fogler (1998)) (Figure 3b.2). In fact, the wormholes tend to widen downstream: as dissolution progresses, the spacing between the active wormholes increases and they focus increasingly more flow. In turn, the flow spreads sideways from the wormhole tip through the highly conductive transverse pores, leading to widening downstream. Analogous widening was also observed in viscous fingering and solidification (Budek et al., 2015; Couder et al., 1990), apparently induced by similar dynamics.

The effect of anisotropy on wormhole shape has also important implications for permeability evolution and the fluid volume to breakthrough curve. The latter is important in oil well stimulation, in which one looks

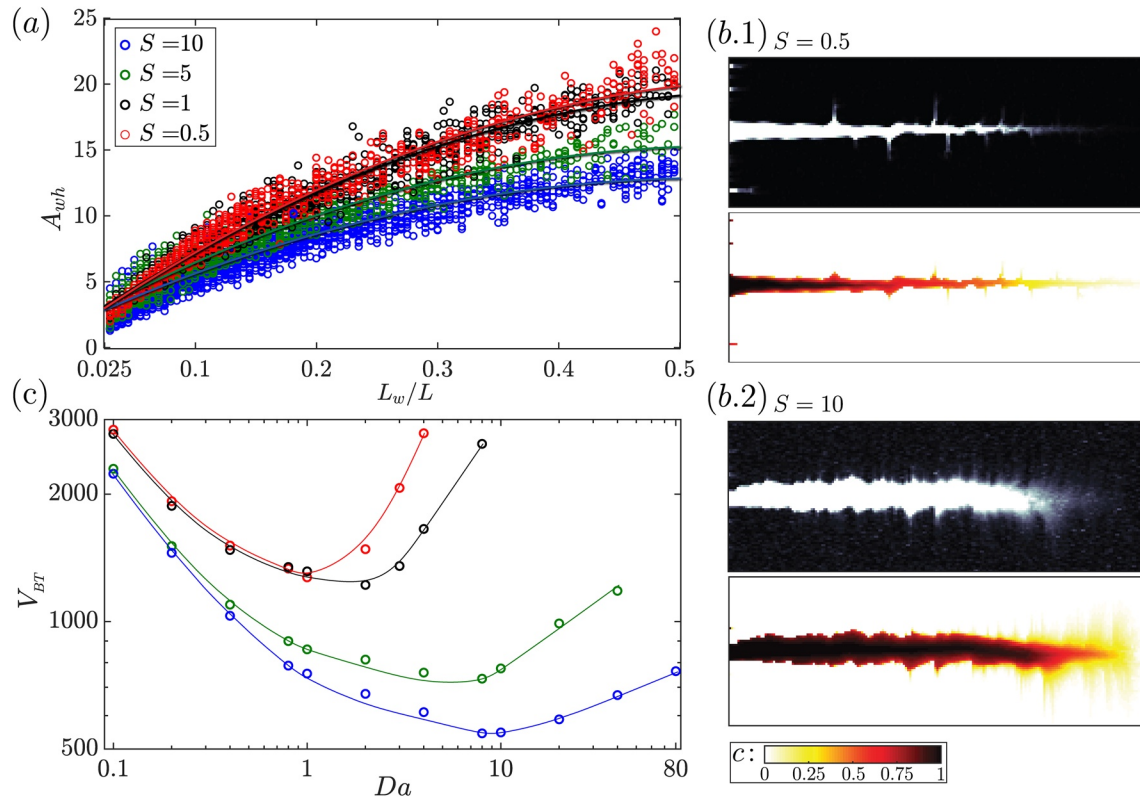


Figure 3. (a) Aspect ratio of the individual wormholes (circles), A_{wh} , defined as wormhole length, L_w over its average width (measured at breakthrough). Lines denote second-order polynomial fits. (b) Magnification of single wormholes (grayscale, white corresponds to fully dissolved regions) and the corresponding reactant concentration field, c . For low S ($S = 0.5$, b.1), reactant concentration decays within the wormhole, resulting in an elongated conical shape and high A_{wh} . Conversely, for $S = 10$ (b.2), the flow rate in the wormholes is higher and wormholes become more linear. (c) Volume to breakthrough, V_{BT} , versus Da . Changing anisotropy shifts the optimum injection rate (lines are guide for the eye connecting the simulation results); in (c) a hundred realizations were carried out on smaller networks (100 nodes in the x -direction).

for an optimum injection rate allowing to attain breakthrough with a minimum reactant usage (Fredd & Fogler, 1998; Xu et al., 2020). This is usually associated with the formation of dominant wormholes because they progress faster than conical ones. Since for larger S dominant wormholes appear at lower flow rates (higher Da), a corresponding shift takes place in the optimum injection rate (Figure 3c).

Lastly, we focus on low S conditions, where wormholes tend to develop pronounced side branches that strongly compete with the main wormhole and occasionally even divert the bulk flow (Figures 1a and 4a.1). To investigate the development of side branches, we use a simple model system with a central permeable pre-existing channel extending from the inlet to $1/4L_x$, with the rest of the pores of almost uniform sizes (relative standard deviation of 0.03). We observe that while in the isotropic system ($S = 1$) hardly any side branches develop, for $S = 0.1$ branching becomes extensive (cf., Figure 4b.2 and 4b.4).

Inspecting the pressure field at $t = 0$ reveals that for $S = 0.1$ the pressure perturbation induced by the preexisting channel decays sharply in the transverse direction (Figure 4b.1, see inset), because of the high resistivity of the transverse pores. Conversely, the pressure decay is much more gradual for isotropic media (Figure 4b.3). These observations reveal that the short screening range at $S = 0.1$, and the pressure gradient that is almost perpendicular to the channel, promote transverse flow and branch development. The branches efficiently drain fluid to the outlet, and their extension continues due to the short transverse screening length and the relatively high transverse pressure gradient. As the process continues, new branches develop downstream from the main wormhole body. Consequently, upstream branches become gradually screened-off and are eventually abandoned. Similar branching was observed at low S conditions in viscous fingering on a lattice and in solidification (Budek et al., 2015; Couder et al., 1990).

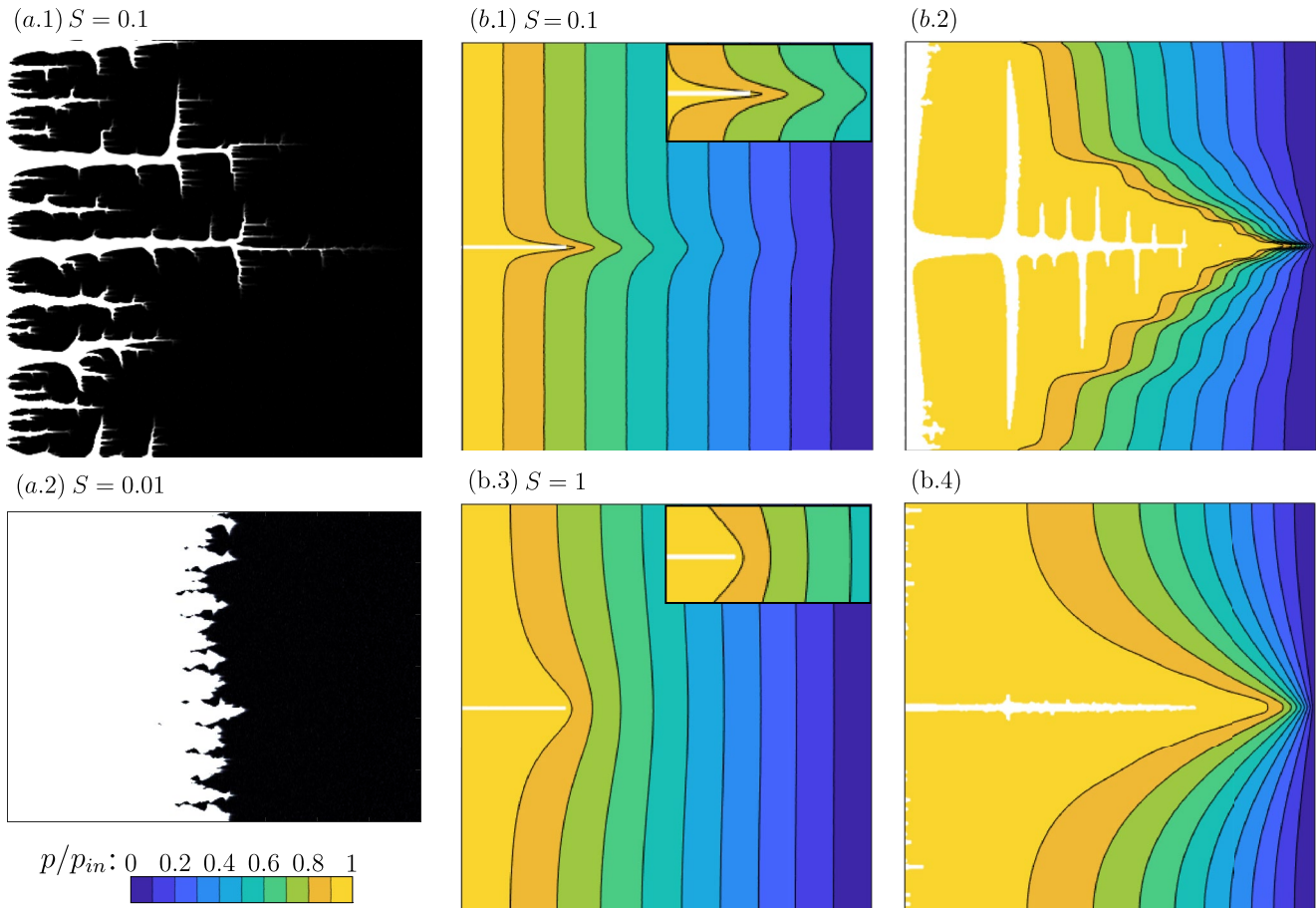


Figure 4. (a) Dissolution patterns at low S (wider longitudinal pores); fully dissolved areas marked in white. For $S = 0.1$ pronounced branches develop (a.1) whereas for lower S , wormholes tend to merge (a.2). (b) Branching development is studied using a system with a seeded central channel (white segments in b.1 and b.3). At $t = 0$ for $S = 0.1$, the pressure perturbation induced by the channel decays sharply, leading to large transverse gradients and short screening range, which promote branching. Conversely, for $S = 1$ extensive screening occurs ahead of the wormhole tip (cf., magnification in b.1 and b.2).

For very narrow traverse pores ($S = 0.01$), the weak competition results in wormhole merging and relatively compact and planar dissolution front. Compact front is commonly a characteristic of low Péclet diffusion-dominated conditions (Golfier et al., 2002, Figure 4a.2). Here, however, we show that at high Péclet, low S conditions can preclude wormholing, which would otherwise develop if the medium was isotropic.

4. Summary

Simulations using a pore network model reveal that the degree of anisotropy S (ratio of transverse to longitudinal pore-sizes) markedly affects wormholing and permeability evolution. In particular, anisotropy alters the wormhole competition and their characteristic spacings and shapes. It also leads to a shift in the optimum injection rate, which is important for practical applications. These findings are comparable with those reported for other unstable growth processes, such as viscous fingering. However, we also find important difference: While in viscous fingering for $S \gtrsim 1$ the spacing between the fingers scales linearly with anisotropy degree S , it does not in wormholing. This could be attributed to the effect of anisotropy on wormhole shape and the link between the latter and the wormhole advancement velocity. The elucidation of these intriguing mechanisms remains the subject of future investigation.

Finally, we note that the anisotropy model adopted here, with different pore diameters in orthogonal directions, represents one of many possible ways of introducing anisotropy in rocks. To test the generality of our results, we have also analyzed the dissolution patterns in a single fracture, with anisotropy introduced by

controlling the spatial correlation length of the aperture in two orthogonal directions. The results presented in SI (S2) show a remarkable agreement with the pore network model, demonstrating that our main conclusions do not depend on the details of pore-scale anisotropy model.

Data Availability Statement

Data in this study are available in (<https://doi.org/10.5281/zenodo.3980615>).

Acknowledgments

Piotr Szymczak was supported by the National Science Centre (Poland) under research Grant 2016/21/B/ST3/01373. Roi Roded acknowledges the Israel Water Authority student's scholarship.

References

- Adler, P. M., Thovert, J.-F., & Mourzenko, V. V. (2013). *Fractured porous media*. Oxford, UK: Oxford University Press.
- Aharonov, E., Whitehead, J. A., Kelemen, P. B., & Spiegelman, M. (1995). Channeling instability of upwelling melt in the mantle. *Journal of Geophysical Research*, *100*(B10), 20433–20450. <https://doi.org/10.1029/95jb01307>
- Algive, L., Bekri, S., & Vizika, O. (2010). Pore-network modeling dedicated to the determination of the petrophysical-property changes in the presence of reactive fluid. *SPE Journal*, *15*(03), 618–633. <https://doi.org/10.2118/124305-pa>
- Alkattan, M., Oelkers, E. H., Dandurand, J.-L., & Schott, J. (1997). Experimental studies of halite dissolution kinetics, 1 The effect of saturation state and the presence of trace metals. *Chemical Geology*, *137*(3–4), 201–219. [https://doi.org/10.1016/s0009-2541\(96\)00164-7](https://doi.org/10.1016/s0009-2541(96)00164-7)
- Barton, N. (2006). *Rock quality, seismic velocity, attenuation and anisotropy*. London, UK: CRC Press. <https://doi.org/10.1201/9780203964453>
- Békri, S., Thovert, J. F., & Adler, P. M. (1995). Dissolution of porous media. *Chemical Engineering Science*, *50*(17), 2765–2791. [https://doi.org/10.1016/0009-2509\(95\)00121-k](https://doi.org/10.1016/0009-2509(95)00121-k)
- Ben-Jacob, E., Godbey, R., Goldenfeld, N. D., Koplik, J., Levine, H., Mueller, T., & Sander, L. M. (1985). Experimental demonstration of the role of anisotropy in interfacial pattern formation. *Physical Review Letters*, *55*(12), 1315–1318. <https://doi.org/10.1103/physrevlett.55.1315>
- Bonnet, E., Bour, O., Odling, N. E., Davy, P., Main, I., Cowie, P., & Berkowitz, B. (2001). Scaling of fracture systems in geological media. *Reviews of Geophysics*, *39*(3), 347–383. <https://doi.org/10.1029/1999rg000074>
- Bruno, M. S. (1994). Micromechanics of stress-induced permeability anisotropy and damage in sedimentary rock. *Mechanics of Materials*, *18*(1), 31–48. [https://doi.org/10.1016/0167-6636\(94\)90004-3](https://doi.org/10.1016/0167-6636(94)90004-3)
- Budek, A., Garstecki, P., Samborski, A., & Szymczak, P. (2015). Thin-finger growth and droplet pinch-off in miscible and immiscible displacements in a periodic network of microfluidic channels. *Physics of Fluids*, *27*(11), 112109. <https://doi.org/10.1063/1.4935225>
- Budek, A., & Szymczak, P. (2012). Network models of dissolution of porous media. *Physical Review E*, *86*(5), 056318. <https://doi.org/10.1103/physreve.86.056318>
- Cabeza, Y., Hidalgo, J. J., & Carrera, J. (2020). Competition is the underlying mechanism controlling viscous fingering and wormhole growth. *Geophysical Research Letters*, *47*(3), e2019GL084795. <https://doi.org/10.1029/2019gl084795>
- Chadam, J., Hoff, D., Merino, E., Ortoleva, P., & Sen, A. (1986). Reactive infiltration instabilities. *IMA Journal of Applied Mathematics*, *36*(3), 207–221. <https://doi.org/10.1093/imamat/36.3.207>
- Clavaud, J.-B., Maineult, A., Zamora, M., Rasolofosaon, P., & Schlitter, C. (2008). Permeability anisotropy and its relations with porous medium structure. *Journal of Geophysical Research*, *113*, B01202. <https://doi.org/10.1029/2007jb005004>
- Colombani, J. (2008). Measurement of the pure dissolution rate constant of a mineral in water. *Geochimica et Cosmochimica Acta*, *72*(23), 5634–5640. <https://doi.org/10.1016/j.gca.2008.09.007>
- Couder, Y., Argoul, F., Arnéodo, A., Maurer, J., & Rabaud, M. (1990). Statistical properties of fractal dendrites and anisotropic diffusion-limited aggregates. *Physical Review A*, *42*(6), 3499–3503. <https://doi.org/10.1103/physreva.42.3499>
- Daccord, G., Liétard, O., & Lenormand, R. (1993). Chemical dissolution of a porous medium by a reactive fluid-II. Convection vs reaction, behavior diagram. *Chemical Engineering Science*, *48*(1), 179–186. [https://doi.org/10.1016/0009-2509\(93\)80294-z](https://doi.org/10.1016/0009-2509(93)80294-z)
- Deng, H., Molins, S., Steefel, C., DePaolo, D., Voltolini, M., Yang, L., & Ajo-Franklin, J. (2016). A 2.5D reactive transport model for fracture alteration simulation. *Environmental Science and Technology*, *50*(14), 7564–7571. <https://doi.org/10.1021/acs.est.6b02184>
- Deng, H., Steefel, C., Molins, S., & DePaolo, D. (2018). Fracture evolution in multimaterial systems: The role of mineral composition, flow rate, and fracture aperture heterogeneity. *ACS Earth and Space Chemistry*, *2*(2), 112–124. <https://doi.org/10.1021/acsearthspacechem.7b00130>
- Detwiler, R. L., & Rajaram, H. (2007). Predicting dissolution patterns in variable aperture fractures: Evaluation of an enhanced depth-averaged computational model. *Water Resources Research*, *43*, W04403. <https://doi.org/10.1029/2006wr005147>
- Dreybrodt, W. (1988). *Processes in karst systems, physics, chemistry, and geology*. Berlin, Heidelberg: Springer. <https://doi.org/10.1007/978-3-642-83352-6>
- Dreybrodt, W., Gabrovšek, F., & Romanov, D. (2005). *Processes of a speleogenesis: A modeling approach*. Postojna, Slovenia: Karst Research Institute ZRC SAZU.
- Filippini, M., Jeannin, P.-Y., & Tacher, L. (2009). Evidence of inception horizons in karst conduit networks. *Geomorphology*, *106*(1–2), 86–99. <https://doi.org/10.1016/j.geomorph.2008.09.010>
- Ford, D., & Williams, P. D. (2013). *Karst hydrogeology and geomorphology*. Chichester, UK: John Wiley & Sons.
- Fredd, C. N., & Fogler, H. S. (1998). Influence of transport and reaction on wormhole formation in porous media. *AIChE Journal*, *44*(9), 1933–1949. <https://doi.org/10.1002/aic.690440902>
- Frumkin, A., Langford, B., Lisker, S., & Amrani, A. (2017). Hypogenic karst at the Arabian platform margins: Implications for far-field groundwater systems. *Geological Society of America Bulletin*, *129*(11–12), 1636–1659
- Fryar, A. E., & Schwartz, F. W. (1998). Hydraulic-conductivity reduction, reaction-front propagation, and preferential flow within a model reactive barrier. *Journal of Contaminant Hydrology*, *32*(3–4), 333–351. [https://doi.org/10.1016/s0169-7722\(98\)00057-6](https://doi.org/10.1016/s0169-7722(98)00057-6)
- Golfier, F., Zarcone, C., Bazin, B., Lenormand, R., Lasseux, D., & Quintard, M. (2002). On the ability of a Darcy-scale model to capture wormhole formation during the dissolution of a porous medium. *Journal of Fluid Mechanics*, *457*, 213–254. <https://doi.org/10.1017/s0022112002007735>
- Hanna, R. B., & Rajaram, H. (1998). Influence of aperture variability on dissolutional growth of fissures in karst formations. *Water Resources Research*, *34*(11), 2843–2853. <https://doi.org/10.1029/98wr01528>
- Hoefner, M. L., & Fogler, H. S. (1988). Pore evolution and channel formation during flow and reaction in porous media. *AIChE Journal*, *34*(1), 45–54. <https://doi.org/10.1002/aic.690340107>

- Huang, Y., Ouillon, G., Saleur, H., & Sornette, D. (1997). Spontaneous generation of discrete scale invariance in growth models. *Physical Review E*, 55(6), 6433–6447. <https://doi.org/10.1103/physreve.55.6433>
- Kang, P. K., Dentz, M., Le Borgne, T., & Juanes, R. (2015). Anomalous transport on regular fracture networks: Impact of conductivity heterogeneity and mixing at fracture intersections. *Physical Review E*, 92(2), 022148. <https://doi.org/10.1103/physreve.92.022148>
- Kang, P. K., Lei, Q., Dentz, M., & Juanes, R. (2019). Stress-induced anomalous transport in natural fracture networks. *Water Resources Research*, 55(5), 4163–4185. <https://doi.org/10.1029/2019wr024944>
- Krug, J., Kassner, K., Meakin, P., & Family, F. (1993). Laplacian needle growth. *Europhysics Letters*, 24(7), 527–532. <https://doi.org/10.1209/0295-5075/24/7/004>
- Lai, K.-H., Chen, J.-S., Liu, C.-W., Hsu, S.-Y., & Steefel, C. (2016). Effect of medium permeability anisotropy on the morphological evolution of two non-uniformities in a geochemical dissolution system. *Journal of Hydrology*, 533, 224–233. <https://doi.org/10.1016/j.jhydrol.2015.11.039>
- Lichtner, P. C. (1991). The quasi-stationary state approximation to fluid/rock reaction: Local equilibrium revisited. In J. Ganguly (Ed.), *Diffusion, atomic ordering, and mass transport: Selected topics in geochemistry*. 452–560. New York, NY: Springer US. https://doi.org/10.1007/978-1-4613-9019-0_13
- Niemi, A., Bear, J., & Bensabat, J. (2017). *Geological storage of CO₂ in deep saline formations*. Dordrecht, Netherlands: Springer.
- Nogues, J. P., Fitts, J. P., Celia, M. A., & Peters, C. A. (2013). Permeability evolution due to dissolution and precipitation of carbonates using reactive transport modeling in pore networks. *Water Resources Research*, 49(9), 6006–6021. <https://doi.org/10.1002/wrcr.20486>
- Palmer, A. N. (1991). Origin and morphology of limestone caves. *The Geological Society of America Bulletin*, 103(1), 1–21. [https://doi.org/10.1130/0016-7606\(1991\)103<0001:oamolc>2.3.co;2](https://doi.org/10.1130/0016-7606(1991)103<0001:oamolc>2.3.co;2)
- Panga, M. K. R., Ziauddin, M., & Balakotaiah, V. (2005). Two-scale continuum model for simulation of wormholes in carbonate acidization. *AIChE Journal*, 51(12), 3231–3248. <https://doi.org/10.1002/aic.10574>
- Peng, C., Crawshaw, J. P., Maitland, G. C., & Trusler, J. P. M. (2015). Kinetics of calcite dissolution in CO₂-saturated water at temperatures between (323 and 373) K and pressures up to 13.8 MPa. *Chemical Geology*, 403, 74–85. <https://doi.org/10.1016/j.chemgeo.2015.03.012>
- Perne, M., Covington, M., & Gabrovšek, F. (2014). Evolution of karst conduit networks in transition from pressurized flow to free-surface flow. *Hydrology and Earth System Sciences*, 18(11), 4617–4633. <https://doi.org/10.5194/hess-18-4617-2014>
- Raoof, A., Nick, H. M., Wolterbeek, T. K. T., & Spiers, C. J. (2012). Pore-scale modeling of reactive transport in wellbore cement under CO₂ storage conditions. *International Journal of Greenhouse Gas Control*, 11, S67–S77. <https://doi.org/10.1016/j.ijggc.2012.09.012>
- Roded, R., Aharonov, E., Holtzman, R., & Szymczak, P. (2020). Reactive flow and homogenization in anisotropic media. *Water Resources Research*, 56, e2020WR027518. <https://doi.org/10.1029/2020WR027518>
- Roded, R., Paredes, X., & Holtzman, R. (2018). Reactive transport under stress: Permeability evolution in deformable porous media. *Earth and Planetary Science Letters*, 493, 198–207. <https://doi.org/10.1016/j.epsl.2018.04.041>
- Roy, A., Roy, S., Bhattacharyya, A. J., Banerjee, S., & Tarafdar, S. (1999). Discrete scale invariance in viscous fingering patterns. *European Physical Journal B*, 12(1), 1–3. <https://doi.org/10.1007/s100510050966>
- Sahimi, M. (2011). *Flow and transport in porous media and fractured rock: From classical methods to modern approaches*. Weinheim, Germany: John Wiley & Sons. <https://doi.org/10.1002/9783527636693>
- Schwalbert, M. P., Zhu, D., & Hill, A. D. (2017). Extension of an empirical wormhole model for carbonate matrix acidizing through two-scale continuum 3D simulations In *SPE Europec featured at 79th EAGE Conference and Exhibition*. paper no. SPE-185788-MS. <https://doi.org/10.2118/185788-ms>
- Steefel, C. I., & Lasaga, A. C. (1990). Evolution of dissolution patterns. In D. C. Melchior, & R. L. Bassett (Eds.), *Chemical Modeling of Aqueous Systems II*. 212–225. American Chemical Society. <https://doi.org/10.1021/bk-1990-0416.ch016>
- Szymczak, P., & Ladd, A. J. C. (2006). A network model of channel competition in fracture dissolution. *Geophysical Research Letters*, 33(5), L05401. <https://doi.org/10.1029/2005gl025334>
- Szymczak, P., & Ladd, A. J. C. (2009). Wormhole formation in dissolving fractures. *Journal of Geophysical Research*, 114, B06203. <https://doi.org/10.1029/2008jb006122>
- Upadhyay, V. K., Szymczak, P., & Ladd, A. J. C. (2015). Initial conditions or emergence: What determines dissolution patterns in rough fractures? *Journal of Geophysical Research: Solid Earth*, 120(9), 6102–6121. <https://doi.org/10.1002/2015jb012233>
- Varloteaux, C., Vu, M. T., Békri, S., & Adler, P. M. (2013). Reactive transport in porous media: Pore-network model approach compared to pore-scale model. *Physical Review E*, 87(2), 023010. <https://doi.org/10.1103/physreve.87.023010>
- Wang, H., Bernabé, Y., Mok, U., & Evans, B. (2016). Localized reactive flow in carbonate rocks: Core-flood experiments and network simulations. *Journal of Geophysical Research: Solid Earth*, 121(11), 7965–7983. <https://doi.org/10.1002/2016jb013304>
- Xu, L., Szymczak, P., Toussaint, R., Flekkøy, E. G., & Måløy, K. J. (2020). Dissolution phase diagram in radial geometry. *Frontiers in Physics*, 8, 369. <https://doi.org/10.3389/fphy.2020.00369>

References From the Supporting Information

- Bejan, A. (2013). *Convection heat transfer*. Hoboken, NJ: John Wiley & Sons. <https://doi.org/10.1002/9781118671627>
- Gupta, N., & Balakotaiah, V. (2001). Heat and mass transfer coefficients in catalytic monoliths. *Chemical Engineering Science*, 56(16), 4771–4786. [https://doi.org/10.1016/s0009-2509\(01\)00134-8](https://doi.org/10.1016/s0009-2509(01)00134-8)
- Hayes, R. E., & Kolaczowski, S. T. (1994). Mass and heat transfer effects in catalytic monolith reactors. *Chemical Engineering Science*, 49(21), 3587–3599. [https://doi.org/10.1016/0009-2509\(94\)00164-2](https://doi.org/10.1016/0009-2509(94)00164-2)
- Noiriél, C., & Deng, H. (2018). Evolution of planar fractures in limestone: The role of flow rate, mineral heterogeneity and local transport processes. *Chemical Geology*, 497, 100–114. <https://doi.org/10.1016/j.chemgeo.2018.08.026>
- Rajaram, H., Cheung, W., & Chaudhuri, A. (2009). Natural analogs for improved understanding of coupled processes in engineered earth systems: Examples from karst system evolution. *Current Science*, 97, 1162–1176.
- Rohsenow, W. M., Hartnett, J. P., & Cho, Y. I. (1998). *Handbook of heat transfer*. New York: McGraw-Hill.
- Saupe, D. (1988). Algorithms for random fractals, in *The science of fractal images* edited by H. Peitgen and D. Saupe (pp 71–136). New York, NY: Springer US. https://doi.org/10.1007/978-1-4612-3784-6_2
- Szymczak, P., & Ladd, A. J. C. (2012). Reactive-infiltration instabilities in rocks. Fracture dissolution. *Journal of Fluid Mechanics*, 702, 239–264. <https://doi.org/10.1017/jfm.2012.174>